Source properties of the 2019 M_L 6.3 Hualien, Taiwan, earthquake, determined by the local strong motion networks

Yen-Yu Lin,[1,2] Yi-Ying Wen [3,4] and Yin-Tung Yen[5]

[1]*Department of Earth Sciences, National Central University, Taoyuan 32001, Taiwan*
[2]*Earthquake-Disaster & Risk Evaluation and Management Center, National Central University, Taoyuan 32001, Taiwan*
[3]*Department of Earth and Environmental Sciences, National Chung Cheng University, Chia-yi County 62102, Taiwan. E-mail: yiyingwen@gmail.com*
[4]*Environment and Disaster Monitoring Center, National Chung Cheng University, Chia-yi County 62102, Taiwan*
[5]*Disaster Prevention Technology Research Center, Sinotech Engineering Consultants, Inc., Taipei 11494, Taiwan*

SUMMARY

The 2019 M_L 6.3 Hualien earthquake struck the northern Longitudinal Valley (LV) and generated not only large strong motions (intensity of 7, as defined by the Central Weather Bureau, Taiwan) locally but also widespread strong shaking in metropolises in northern Taiwan. In this study, we analyse strong motion records from local seismic networks to understand the source properties of the 2019 event. We first obtain the centroid location of the 2019 event using the source-scanning algorithm (SSA) technique by applying the unfiltered records. The determined centroid location is 121.55°E, 24.10°N, with a depth of 22.5 km. This location is 5.5 km north–northwest of and 3.8 km deeper than the Central Weather Bureau hypocentre, suggesting that the 2019 event occurred on the high-angle west-dipping plane of the focal solution. The centroid time delay is 3.35 s. Then, we obtain strong motion generation areas (SMGAs) of the 2019 event using the empirical Green's function method by considering the broad-band waveforms (0.4–10 Hz). Unlike other moderate-sized earthquakes in Taiwan, which have one SMGA, we determine that there were two SMGAs in the 2019 event. SMGA1 initiated at the CWB hypocentre with a size of 4.00 km^2, and SMGA2 initiated at the centroid location determined by the SSA approach with a size of 3.63 km^2. Such small areas cause high stress drops of 13.7 and 27.4 MPa for SMGA1 and SMGA2, respectively. We infer that the localized high stress drop of SMGAs is one of the important factors responsible for high peak-ground accelerations (PGAs) in Taiwan in addition to a strong directivity effect coupled with the radiation pattern reported by the previous study. Furthermore, previous moderate-sized earthquakes on an active structure called the Xiulin segment revealed similar source properties with a high stress drop and generated large PGA locally as well as in the metropolises of northern Taiwan. Considering the stored moment deficit, the probability of a future large earthquake in the northern LV region remains high. It is essential to consider seismic hazard assessment and mitigation for this not-well-known but high-seismic-potential region.

Key words: Earthquake ground motions; Earthquake hazards; Earthquake source observations.

1 INTRODUCTION

An M_L 6.3 earthquake occurred in eastern Taiwan on 2019 April 18. This moderate earthquake (hereafter, the 2019 event) not only generated extremely large shaking (intensity of 6–7) near the hypocentre but also produced strong ground motion (intensity of 4) in metropolises in northern Taiwan. The epicentral distance was approximately 100 km from cities such as Taipei, New Taipei and Taoyuan Cities (Fig. 1a). One death, 16 injuries and some minor

damage were reported (CEOC 2019; NCREE 2019; Su 2019). The hypocentre was located at 121.56°E, 24.05°N with a focal depth of 18.8 km, as reported by the Central Weather Bureau (CWB). The moment tensor solution of the CWB revealed that the mechanism of the 2019 event was a thrust with minor strike-slip motion, and the aftershock distribution was clustered on a high-angle west-dipping fault plane (Fig. 2; Table 1).

Lee *et al*. (2020) obtained a significant difference in the peak-ground acceleration (PGA) distribution in northern Taiwan of the
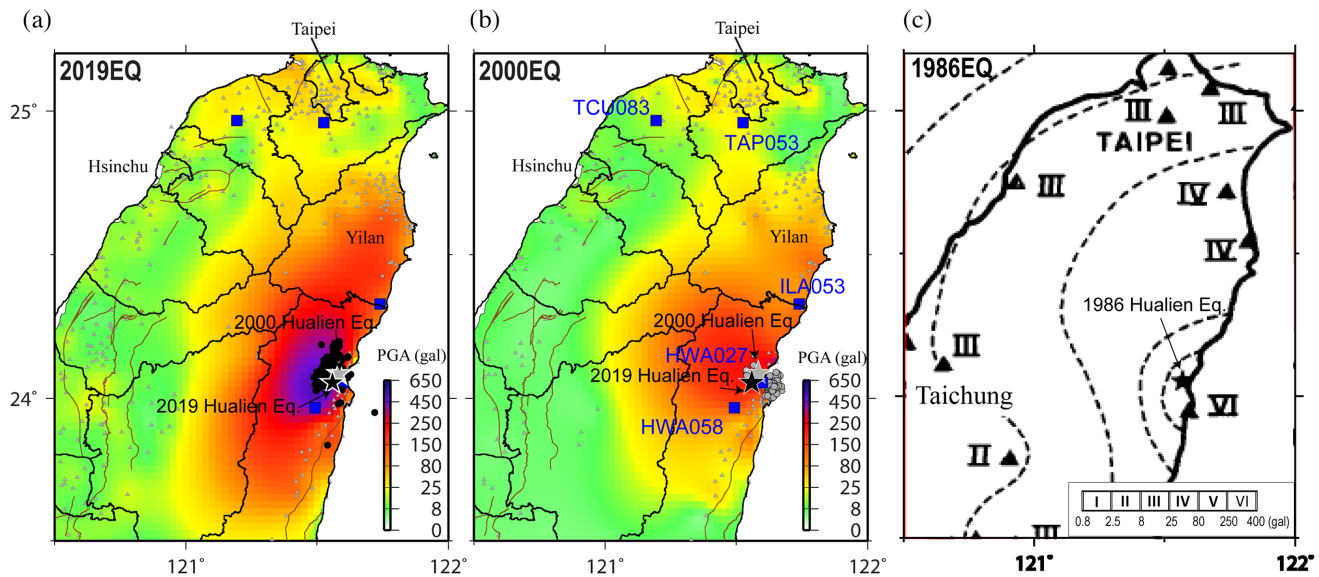
Figure 1. The observed peak ground acceleration determined from free-field strong motion stations (triangles and squares) of (a) the 2019 Hualien earthquake and (b) the 2000 Hualien earthquake. (c) The isoseismal map of the 1986 Hualien earthquake, modified from Tsai *et al*. (1986).

2019 event, and a nearby event occurred in 2018 with a similar magnitude (fig. 2 in Lee *et al*. 2020). They provided principal information on the overall faulting process by applying finite-fault modelling with low-frequency band data (0.05–0.33 Hz). They concluded that the widespread strong ground shaking generated by the 2019 event was attributed to a strong northward directivity effect coupled with its source radiation pattern during faulting. They obtained a small asperity located at the hypocentre, and a larger asperity occurred 10 km north of the hypocentre (fig. 4 in Lee *et al*. 2020).

The northern Longitudinal Valley (LV), which overlies the suture zone between the Philippine Sea plate and the Eurasian plate, extends 150 km between Hualien and Taitung in eastern Taiwan (Yu & Kuo 2001; Hickman *et al*. 2002). In recent decades, the northern LV has been struck by several large disastrous events (Fig. 2). These events were the 1951 Longitudinal Valley earthquake sequence, the 1986 M6.5 Hualien earthquake, the 2000 *M*6.1 Hualien earthquake, the 2003 *M*6.4 Cheng Kung earthquake, the 2013 *M*6.4 Ruisui earthquake and the 2018 *M*6.4 Hualien earthquake (Ching *et al*. 2007; Chen *et al*. 2008; Lee *et al*. 2014; Wen *et al*. 2019). To date, this region still has several faults with a high rupture probability from the Taiwan earthquake model (TEM), such as the Milun and LV faults (Wang *et al*. 2016; Chan *et al*. 2017, 2019). Not surprisingly, approximately 14 months after the 2018 Hualien earthquake (the '2018 event'), the 2019 event again struck the northern LV region, a locked zone with high potential for a large earthquake (Rau *et al*. 2007). Although the distance between the epicentres of these earthquakes is only ~20 km, the damage patterns of the two events are very different. The 2018 event caused serious damage in Hualien City to the south of the epicentre (Huang & Huang 2018; Kuo *et al*. 2019; Lee *et al*. 2019; Lo *et al*. 2019; Wen *et al*. 2019; Lin *et al*. 2020), while the 2019 event significantly affected cities 100 km away in northern Taiwan (Fig. 1a).

Studying the seismic source properties of a large earthquake using a dense strong-motion station network is powerful due to the high-resolution records and good station coverage. Lin *et al*. (2018) identified two clear subevents of the 2016 *M*L 6.6 Meinong, Taiwan

earthquake by analysing unfiltered records of a local dense network and successfully simulated the high-velocity pulse (>100 cm s^{-1}) that had damaged the city. In addition, Lin *et al*. (2020) analysed the waveforms from a local dense array and found that slips on a short local patch (i.e. the Milun fault) of the 2018 Hualien earthquake generated a strong velocity pulse that was the dominant cause of damage in Hualien City. These velocity pulses are difficult to explain using finite-fault modelling due to the use of an insufficient velocity model without considering precise site effects (Lin *et al*. 2020). On the other hand, Irikura (1986) developed an empirical Green's function (EGF) method to simulate broad-band strong-motion records (up to 10 Hz), which assumed a characterized source model consisting of one or more rectangular patches. Miyake *et al*. (2001, 2003) named the patch the 'strong motion generation area (SMGA),' which is a characteristic area with a uniform slip and stress drop within the total rupture area. With the advantage of a dense strong-motion station network in Taiwan, several moderate-to-large events have been well studied using the EGF method, including eight Nantou events that occurred in 1999 and 2013 (Wen *et al*. 2017), the 2013 Ruisui event (Wen *et al*. 2016), and the 2010 Jiashian and 2016 Meinong earthquakes (Wen *et al*. 2020). These blind fault events in Taiwan were found to follow a particular self-similar scaling relationship, showing a small dimension of SMGA and a high stress drop, which could be attributed to the immature buried fault. Here, we focus on investigating the source properties of the 2019 event using local strong motion networks through analyses in the broad-band range (0.4 to 10 Hz) using the EGF method to better understand the source characteristics and details.

2 DATA

We use seismic records of two strong motion networks, both with accelerometers, in eastern Taiwan (Fig. 3). The first network is the Taiwan Strong Motion Instrumentation Program (TSMIP) network managed by CWB and deployed in a free field (Liu *et al*.
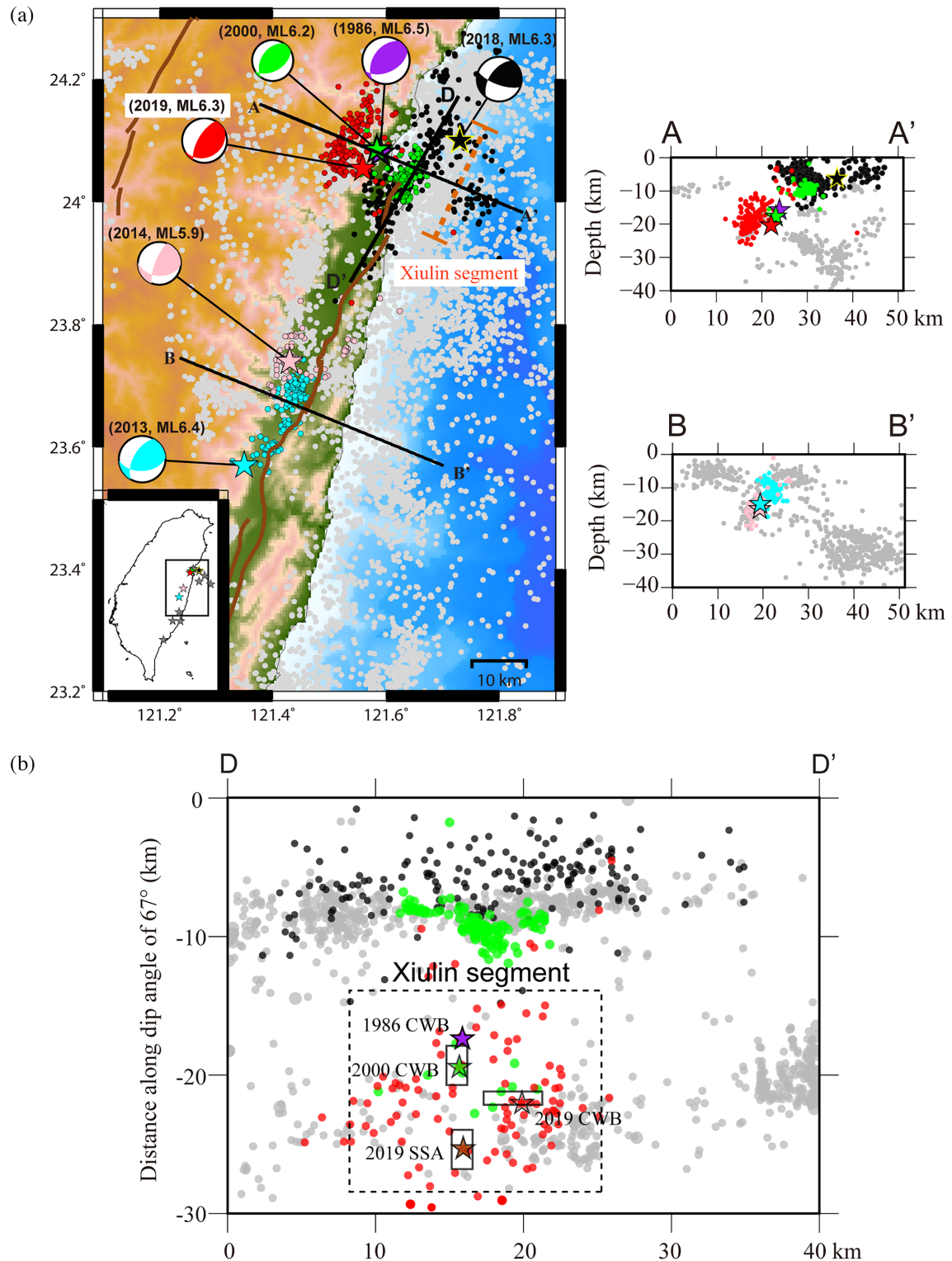
Figure 2. (a) Distribution of earthquakes along the Longitudinal Valley. Epicentres (stars), focal mechanisms and the related aftershock distributions (dots) of different events are shown in various colours: red indicates the 2019 Hualien earthquake; black indicates the 2018 Hualien event; pink indicates the 2014 Fanglin event; blue indicates the 2013 Ruisui event; green indicates the 2000 Hualien event; and purple indicates the 1986 Hualien earthquake. Grey stars and dots indicate the 1951 Longitudinal Valley earthquake sequence, the 2003 Cheng Kung earthquake and background seismicity. The active faults (thick lines) identified by the Central Geological Survey of Taiwan are also shown. (b) The D–D' profile is the cross-section with a dipping angle of 67°. The rectangles indicate the SMGA of the 2000 Hualien earthquake (green star) and SMGA1 (red star), as well as SMGA2 (brown star) of the 2019 Hualien event.

Table 1. Earthquake parameters for the 1986, 2000 and 2019 Hualien earthquakes and the EGF event.

Date	15 Apr 2019 (EGF event)	18 Apr 2019	10 Sep 2000	20 May 1986
Epicentre	121.520°E	121.559°E	121.584°E	121.590°E
	24.045°N	24.054°N	24.085°N	24.080°N
Depth	20.03 km	20.33 km	17.74 km	15.82 km
Fault plane (strike, dip and rake)	210/56/71[a]	210/67/76[a]	214/58/69[b]	214/45/67[d]
M_0	4.64×10^{14} Nm[b]	2.34×10^{18} Nm[c]	5.83×10^{17} Nm[c]	2.40×10^{18} Nm[d]
M_L	4.2	6.3	6.2	6.5

The epicentres were determined by CWB. The seismic moment and fault plane solutions were determined by a: CWB; b: BATS; c: Global CMT solution; and d: U.S. Geological Survey.
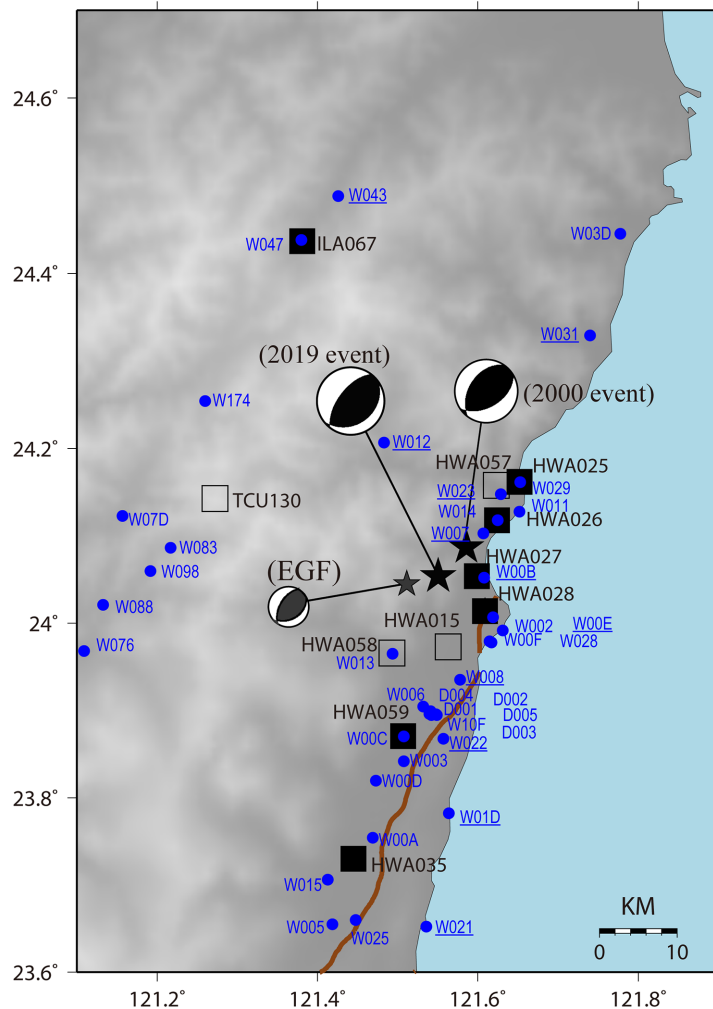

Figure 3. Distribution of the strong motion stations, the 2000 and 2019 Hualien earthquakes and the EGF event. Epicentres (stars) and focal mechanisms of the 2000 and 2019 events and the EGF event are listed in Table 1. Squares indicate TSMIP stations, with open squares showing the stations used in the source spectral ratio analysis and EGF simulation. Dots show the P-Alert stations.

1999; Liu & Tsai 2005). Some TSMIP stations do not have accurate time information. The second network is the P-Alert network operated by National Taiwan University for early warning purposes (Wu *et al.* 2013). The instruments of the P-Alert network were installed in buildings in schools, and their clocks were auto calibrated via the internet. The P-Alert data are used to determine the centroid location only due to its non-free-field characteristic.

3 CENTROID LOCATION DETERMINED BY THE SSA TECHNIQUE

To determine the centroid location of the 2019 event, we apply the source-scanning algorithm (SSA) technique to the P-Alert records (Kao & Shan 2004). This technique was applied broadly in previous studies to determine various source location types, including earthquakes, tremors, and landslides (Kao & Shan 2004, 2007; Kao
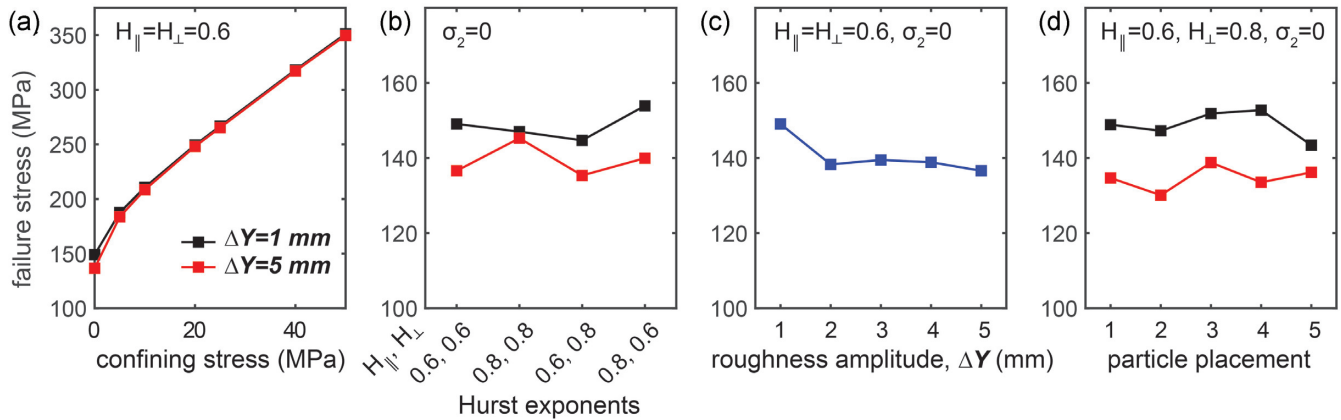
Figure 4. (a) The centroid location determined by the SSA approach. The blue squares demonstrate the centroid location. The circles and diamonds indicate the hypocentres reported by the CWB and obtained by the 3-D velocity structure used in the present study (Huang *et al.* 2014), respectively. The grey grid graph represents the area for the SSA approach. The colour scale shows the marginal probability. (b) Marginal probability of the delay time. The maximum probability is marked with an open circle at 3.35 s.

et al. 2008; Liao *et al.* 2012). Additionally, it has been shown to be efficient for delineating the source characteristics of earthquake doublets (Kan *et al.* 2010) and for determining the centroid location of an earthquake (Lin *et al.* 2018; Lin *et al.* 2020).

The SSA method determines the optimal distribution of a source location using a grid-search method based on the observed waveforms. We follow the procedure for the SSA technique described in Lin *et al.* (2018) and calculate the brightness of an assumed source point (η) at a specific delay time (τ) as

$$\mathrm{br}(\eta, \tau) = \prod_{n=1}^{N} \sum_{m=-M}^{M} \left| P_n(\tau + t_{\eta n} + m\mathrm{d}t) \right|, \quad (1)$$

where P_n is a probability density function (PDF) determined from a seismic waveform n; N is total PDFs used in the SSA approach; $t_{\eta n}$ is the predicted *S*-wave travel time based on a source point η and a station for the waveform n; and dt and $2M$ are the time interval and the number of data points in a window around the arrival time, respectively. The centroid location is determined to be in the location of maximum brightness. Here, we calculate a PDF from a seismic waveform. We integrate an acceleration waveform to a displacement waveform, square the amplitudes, and scale the amplitude function so that the area beneath the function equals one. A high pass filter with a corner of 0.1 Hz is applied. More details of the SSA technique are demonstrated in Lin *et al.* (2018).

In this study, we use 80 waveforms in the horizontal components from 40 P-Alert stations located within a 50 km radius of the CWB epicentre for the SSA analysis. We calculate the *S*-wave predicted arrival time using a 3-D velocity structure in Taiwan (Huang *et al.* 2014). The considered time window is ±1.0 s from the predicted arrival time, and dt is 0.01 s. The potential source region for a grid search spans longitudes 121.30°E to 121.80°E and latitudes 23.75°N to 24.25°N with a 0.025° interval in both directions. The depth ranges from 0.0 to 30.0 km with a 2.5 km grid size. The delay time ranges from 0.0 to 20.0 s with a 0.05 s interval.

The determined centroid location of the Hualien earthquake is 121.55°E ± 2.5 km and 24.10°N ± 1.25 km (Fig. 4). The focal depth is 22.5 km, with considerable uncertainty from 20.0 to 27.5 km. The delay time is approximately 3 s. We have more significant confidence in the horizontal location of the centroid than in its depth, as shown in Fig. A1. Details of the uncertainty of location estimation are described in Appendix A. Fig. 5 indicates the

predicted *P*- and *S*-wave arrival times from the CWB hypocentre (T1 and T2 bars) and the centroid location (T3 and T4 bars) on the N–S record section. The predicted *S*-wave arrivals generated by the centroid location (T4 bar) match the maximum amplitude of the displacement waveforms, suggesting that the obtained centroid location is reasonable. The determined centroid location is 5.5 km to the north–northwest and 3.8 km deeper than the CWB hypocentre (Fig. 4). If slips occurred on a single fault plane, the relative location of the hypocentre and the centroid could be a hint for identifying the exact rupture plane and directivity of an earthquake. We recognize that the rupture of the 2019 event extends from the hypocentre to a more northern and deeper portion along the high-angle west-dipping nodal plane, and the aftershock distribution also supports our observations.

4 STRONG MOTION GENERATION AREAS (SMGA) OF THE 2019 EVENT

To investigate the source properties of the 2019 event, we select an M_L 4.2 event as an EGF with a focal mechanism and a location similar to those of the 2019 event (Fig. 3; Table 1). We then apply the EGF method (detailed in Appendix B) using the TSMIP records in different azimuths near the hypocentre (squares in Fig. 3). The frequency in the calculations ranges from 0.4 to 10 Hz. We select the high-angle west-dipping plane (Table 1) as the rupture plane based on the results of the SSA in Section 3.

Previous studies reproduced the synthetic near-source strong motions, effectively explaining the observed records of the 2013 M_L 6.4 Ruisui and 2014 M_L 5.9 Fanglin earthquakes using a single-SMGA model (Wen *et al.* 2016; Wen 2018). We first assume a single-SMGA model and perform a grid search to obtain optimal SMGA-related parameters, as described by Miyake *et al.* (1999, 2003), by simulating the waveforms to fit the observed displacements and the envelopes of the observed accelerations. The optimal size of a single SMGA is 5.76 km², and the other parameters are shown in Table 2. The starting point of rupture is set at the CWB hypocentre. The comparison of the observed and synthetic waveforms is shown in Fig. 6. The light grey lines display the synthetic waveforms of the single-SMGA model at the stations. We recognize that the synthetics explain only the first few seconds of observations
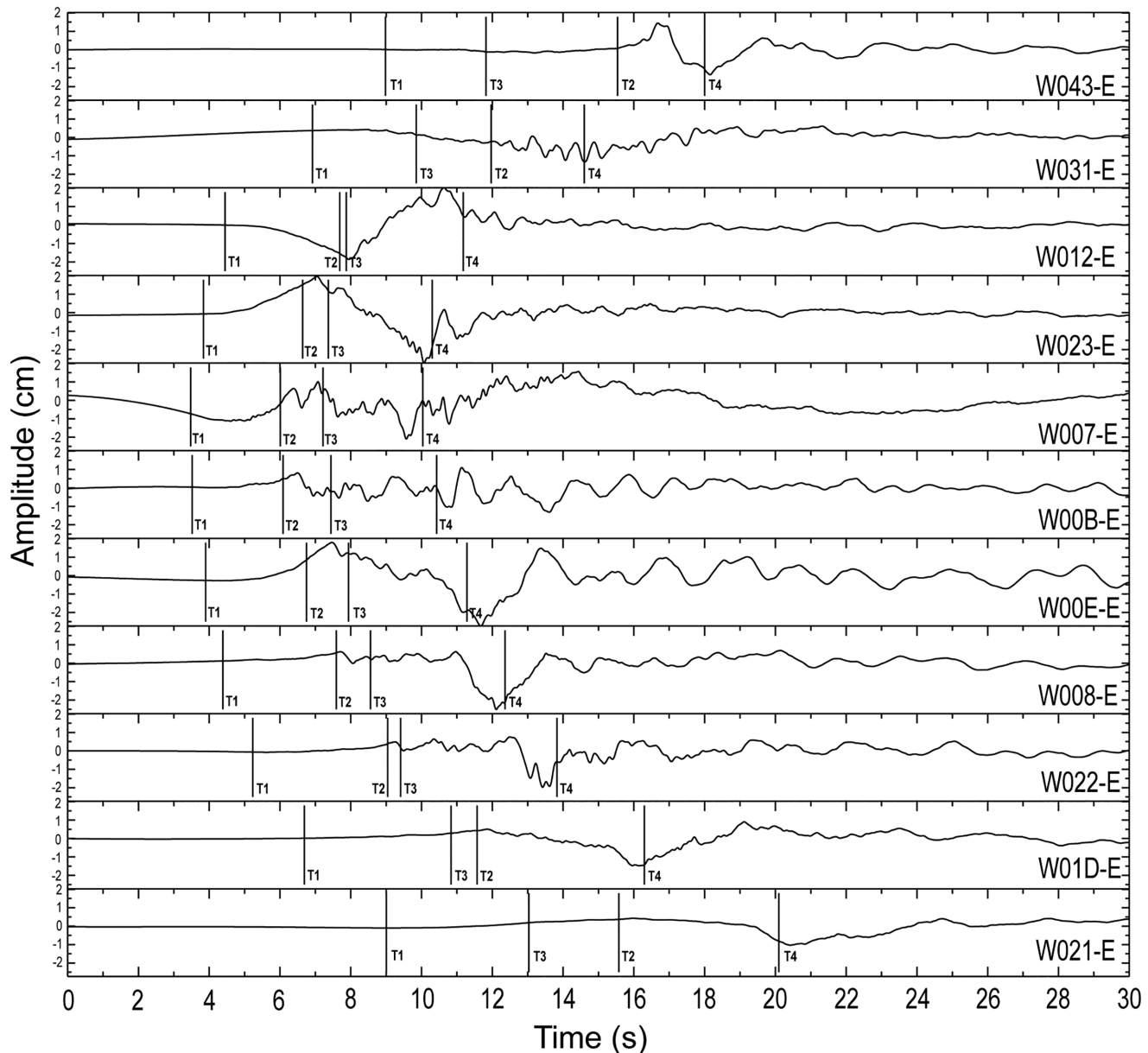
Figure 5. Displacement waveforms of the E–W component in the N–S record section. The stations are marked by underlines in Fig. 3. The T1 and T2 bars show the *P* and *S* phases from the CWB hypocentre, respectively. The T3 and T4 bars demonstrate the *P* and *S* phases generated from the centroid location determined by the SSA approach in Fig. 4, respectively.

Table 2. Parameters of the single SMGA model for the 2019 Hualien earthquake, determined by the strong ground motion simulation.

M_0 (10^{17} Nm)	K	C[a]	Rupture starting Point[b]	L[c] (km)	W[d] (km)	V_r (km s^{-1})	τ_r[e] (s)	S[f] (km^2)	SMGA (km^2)	$\Delta\sigma_{SMGA}$[g] (MPa)
3.76	12	0.470	(6, 7)	2.4	2.4	3.13	0.48	53.96	5.76	21.7

[a]Stress drop ratio between target and EGF events.
[b]Rupture starting point defined as the initiation number of *K* (fault dimension ratio) along the strike and dip, respectively.
[c]Length of the strong motion generation area (SMGA).
[d]Width of the SMGA.
[e]Rise time for the mainshock.
[f]The rupture area estimated from the recipe of Irikura & Miyake (2011).
[g]Stress drop of the SMGA.

with similar phases but overestimated amplitudes. Moreover, the synthetic waveforms of the single-SMGA model are insufficient for describing the later portion with more enormous energy, especially for the acceleration records.

To address this, we further consider a model with two SMGAs for the 2019 event. We set the starting points of rupture for the first SMGA ('SMGA1') and for the second SMGA ('SMGA2') at the CWB hypocentre and the SSA centroid determined in Section
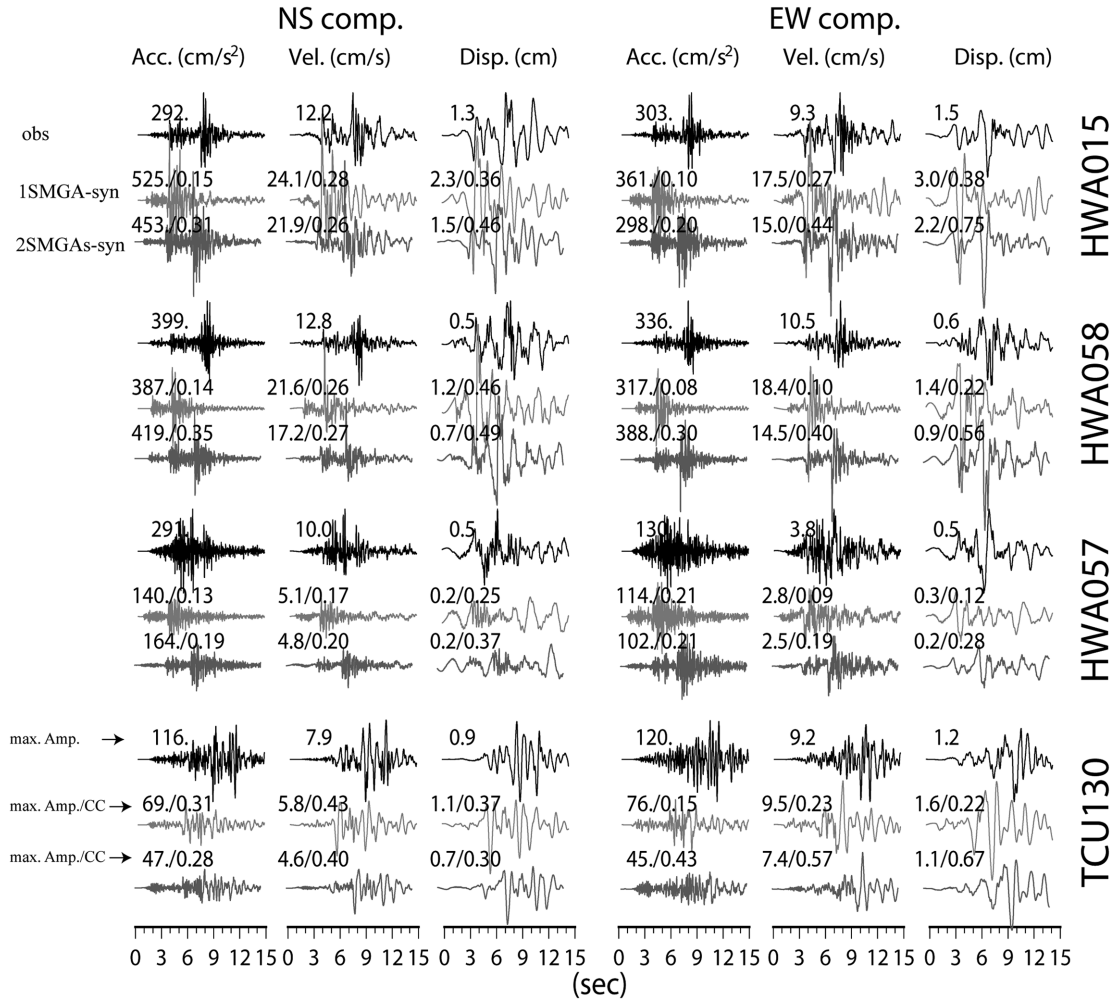
Figure 6. Comparison of the observed (black lines) and synthetic (grey lines) waveforms of the 2019 Hualien earthquake at strong motion stations used for source modelling in the empirical Green's function method (open squares in Fig. 3). The maximum amplitudes (max. Amp.) and the cross-correlation coefficient (CC) of the synthetic and observed data are shown above the traces. 'obs' shows the observed record, '1SMGA-syn' shows the simulation from the single SMGA model and '2SMGAs-syn' shows the simulation from the two SMGAs model.

Table 3. Parameters of the 2-SMGAs model for the 2019 Hualien earthquake determined by the strong ground motion simulation.

	M_0 (10^{17} Nm)	K	C	Rupture starting point	L (km)	W (km)	V_r (km s^{-1})	τ_r (s)	S (km^2)	SMGA (km^2)	$\Delta\sigma_{SMGA}$ (MPa)
SMGA1	1.09	10	0.235	(7, 9)	4.0	1.0	2.58	0.5	23.61	4.00	13.7
SMGA2	2.68	11	0.434	(6, 6)	1.65	2.2	3.16	0.55	43.00	3.63	27.4

3, respectively. We use the first few seconds of observations to obtain the parameters of SMGA1, as listed in Table 3. Since we used the same EGF event, we could rewrite eq. (B2) in Appendix B as

$$\frac{M_0\_sum}{m_0} = C_{sum}K_{sum}^3 = \frac{M_0\_1 + M_0\_2}{m_0} = C_1K_1^3 + C_2K_2^3. \quad (2)$$

We assume that the parameters of the single-SMGA model represent the total response of two SMGAs. Therefore, as we obtain C_1 and K_1 of SMGA1, we can then derive C_2 and K_2. Applying the optimal parameters of SMGA1 with the delay time derived by the SSA analysis, the other parameters of SMGA2 are then determined through the grid search, as listed in Table 3. The results suggest that the simulated waveforms from the 2-SMGAs model (dark grey lines in Fig. 6) explain the observations significantly better than the simulated waveforms from the single-SMGA model. We further

calculate the waveforms at the other stations near the hypocentre (solid square in Fig. 3). The simulated waveforms also explain the observations well (Fig. 7), suggesting that the 2019 event had two SMGAs, as shown in Fig. 2(b). The sizes of SMGA1 and SMGA2 are 4.00 and 3.63 km^2, respectively.

5 DISCUSSION

5.1 High stress drop on asperities of the 2019 event

Miyake *et al.* (2003) analysed several moderate-sized earthquakes in Japan and found that the scaling of the SMGA to the seismic moment (solid circles in Fig. 8) was similar to the scaling of the asperity to the seismic moment obtained based on inversion models (squares in Fig. 8; Somerville *et al.* 1999). However, the combined dimension of the 2-SMGAs model of the 2019 event (solid star
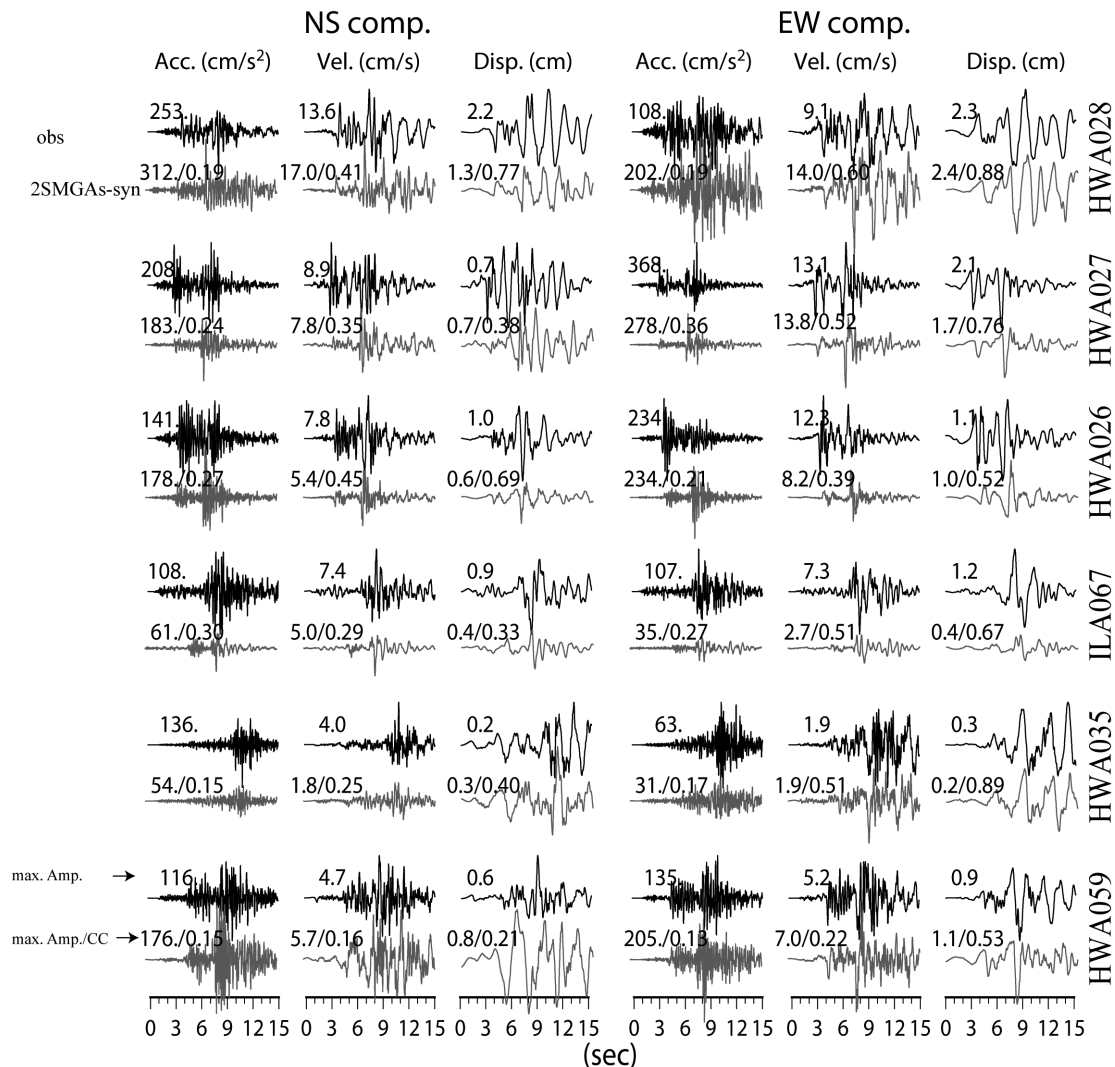
Figure 7. Comparison of observed (black lines) and synthetic (grey lines) waveforms of the 2019 Hualien earthquake at strong motion stations used for forward ground motion simulations (solid squares in Fig. 3). The maximum amplitudes (max. Amp.) and the cross-correlation coefficient (CC) of the synthetic and the observed data are shown above the traces. 'obs' shows the observed record and '2SMGAs-syn' shows the simulation from the two SMGAs model.

in Fig. 8) is much smaller than what is predicted by the empirical relationship indicated by Somerville *et al.* (1999). Nevertheless, it still follows the scaling of the buried earthquakes in the Nantou area and the shallow intraslab earthquakes in Japan, marked as diamonds and open circles in Fig. 8, respectively (Asano *et al.* 2003; Wen *et al.* 2017). Using the scaling parameters *C* and *K*, which are the ratios of the stress drops and fault dimensions between the target event and the EGF event, the seismic moment of each SMGA patch can be calculated by multiplying the moment of the EGF event by CK^3 (Irikura 1986; Miyake *et al.* 2003). The seismic moment of the EGF event determined by the Broadband Array in Taiwan for Seismology (BATS) is 4.64×10^{14} Nm. We then follow the approach of Irikura & Miyake (2011) to estimate a high stress drop in each SMGA and obtain values of 13.7 MPa on SMGA1 and 27.4 MPa on SMGA2 for the 2019 event (Table 3). Events with such a high stress drop are common, especially when events occur on a blind fault at depth. Asano & Iwata (2011) found that, for inland crustal earthquakes in Japan, the stress drops on asperities

increase with depth and that buried asperities have larger stress drops than surface-breaking asperities. Wen *et al.* (2017) showed that moderate blind-fault earthquakes in the Nantou area in Taiwan exhibited high and focal-depth-dependent stress drops. Radiguet *et al.* (2009) and Somerville (2003) found that buried faults strengthen ground shaking.

The finite-fault model of Lee *et al.* (2020), which applies low-frequency data, suggests that a strong directivity effect coupled with the radiation pattern produced intense ground shaking of the 2019 event due to a rupture velocity of ~ 4 km s^{-1} approaching the *S*-wave speed in the source area. However, after analysing high-frequency ground-motion signals, we infer that the high stress drop was localized in small SMGAs of the 2019 event. This is another critical factor in generating such a large amplitude of ground motions in Taiwan since the PGA is proportional to the stress drop (Yen & Ma 2011; Cotton *et al.* 2013). It is helpful to understand the source properties of an earthquake in detail from high-frequency local records.
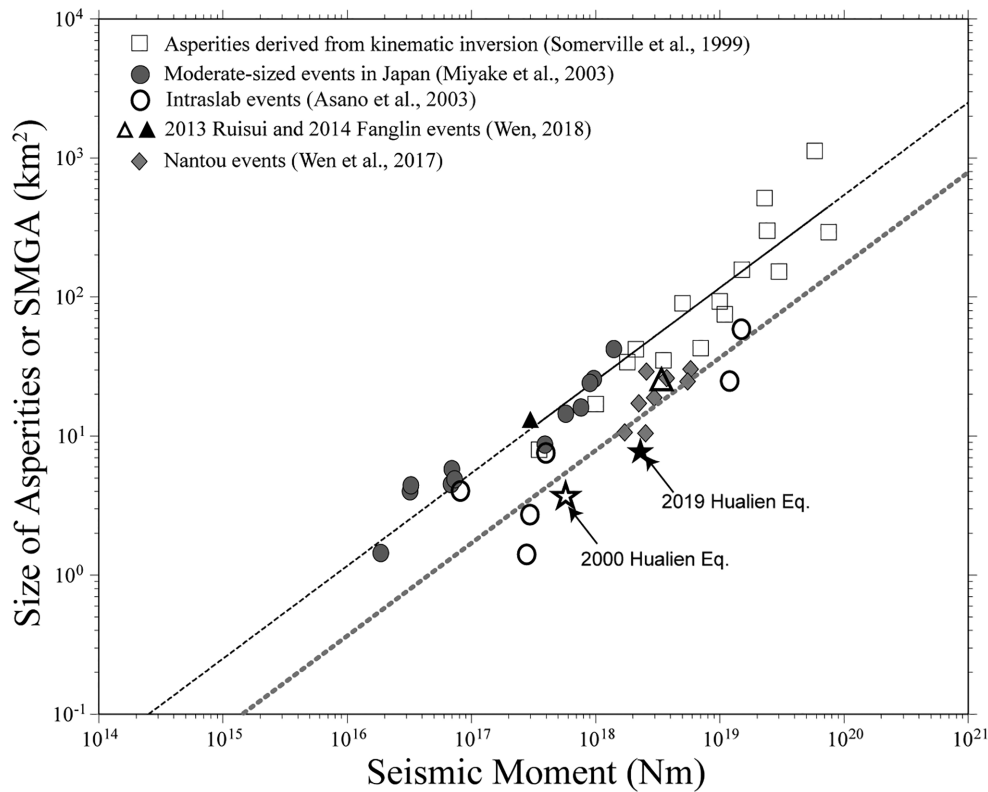
Figure 8. The scaling relation of the seismic moment versus the size of SMGA. The solid line represents the empirical relation between the combined area of the asperities and the seismic moment for the inland crustal earthquakes (Somerville *et al.* 1999), with the dashed lines as the extension for the larger and smaller events. The dotted line indicates the empirical relation of Somerville *et al.* (1999) with a fivefold stress drop. Open and solid stars show our results of the 2000 Hualien earthquake and the combined dimension of the 2-SMGAs model for the 2019 Hualien earthquake, respectively.

5.2 A seismogenic structure generating M6+ events with a high stress drop

In the last 35 yr, three moderate earthquakes in the study area caused damage or high intensity shaking in the metropolises in northern Taiwan. These events occurred in 1986, 2000 and 2019 with M_L 6.5, 6.2 and 6.3, respectively, and with very similar focal mechanisms (Fig. 2). Their hypocentres were not reported at the same point, but all were located on a west-dipping seismogenic structure (Fig. 2). Chen *et al.* (2020) analysed 202 repeating earthquake sequences (RES) with M_L 2.0–4.6 in eastern Taiwan and found that, for the northern LV region, the quasi-periodic RES occurred mostly along the west-dipping Central Range Fault (CRF) at depths greater than 15 km. They also pointed out that the fault segment in this region crept with a stable slip rate of 4.3 cm yr^{-1} at depths of 15–25 km. Such a high slip rate indicates that the fault segment here is very active. The structure that generates these M6 + earthquakes is a part of the fault segment discussed in Chen *et al.* (2020), called the Xiulin segment hereafter (Fig. 2). Since these M6+ events had similar locations, magnitudes, mechanisms, and regular occurrence intervals (14–20 yr), we are curious about the relationship between these M6+ events. In the following, we focus on the comparisons of the waveform similarity for these events and the spatial distribution of the related SMGAs.

Generally, seismologists identify a repeating cluster by analysing waveform similarity. However, it is difficult to follow this approach for these M6+ events since the 2019 event with two SMGAs described in Section 4 generated more complex waveforms (e.g. the

observed waveforms at station HWA015 in Fig. 6). To avoid contamination from the SMGA2 waveforms of the 2019 event, we calculate the cross-correlation coefficient (CC) between the EW-component waveforms of the 2000 and 2019 events for some stations with a 3.5 s window after the *P*-arrival. The frequency range is 2–8 Hz. The results show high agreement of these waveforms (Fig. 9a). This suggests that they nucleated and grew up on the same fault segment (i.e. the Xiulin segment) with a similar focal mechanism. Due to the lack of strong motion records at the same stations for the 1986 event, we cannot make the waveform comparison described above. However, in addition to the consistency of the source parameters (i.e. location, magnitude and mechanism), the comparable strong motion patterns of these events (Fig. 1) imply that these M6+ earthquakes may have similar source properties.

To understand the spatial distribution of SMGAs for these events, we apply the EGF method described in session 4 for the 2000 event. The obtained SMGA-related parameters are listed in Table 4. Fig. 10 shows the comparison of the observed records of the 2000 event and the synthetic waveforms. Most stations exhibit high CCs for the velocity and displacement records. We should mention that, for the 2000 event, only one SMGA is sufficient to explain the observations. The stress drop of its SMGA is still a high value of 24.4 MPa (Table 4). When looking at the unfiltered records of both events (Fig. 9b), the waveforms of farther stations (e.g. ILA053, TAP053 and TCU083, with station locations shown as squares in Fig. 1) display high agreement; however, the waveforms of near-source stations (e.g. HWA027 and HWA058) reveal the difference that the 2019 event exhibits one more wave packet than does the
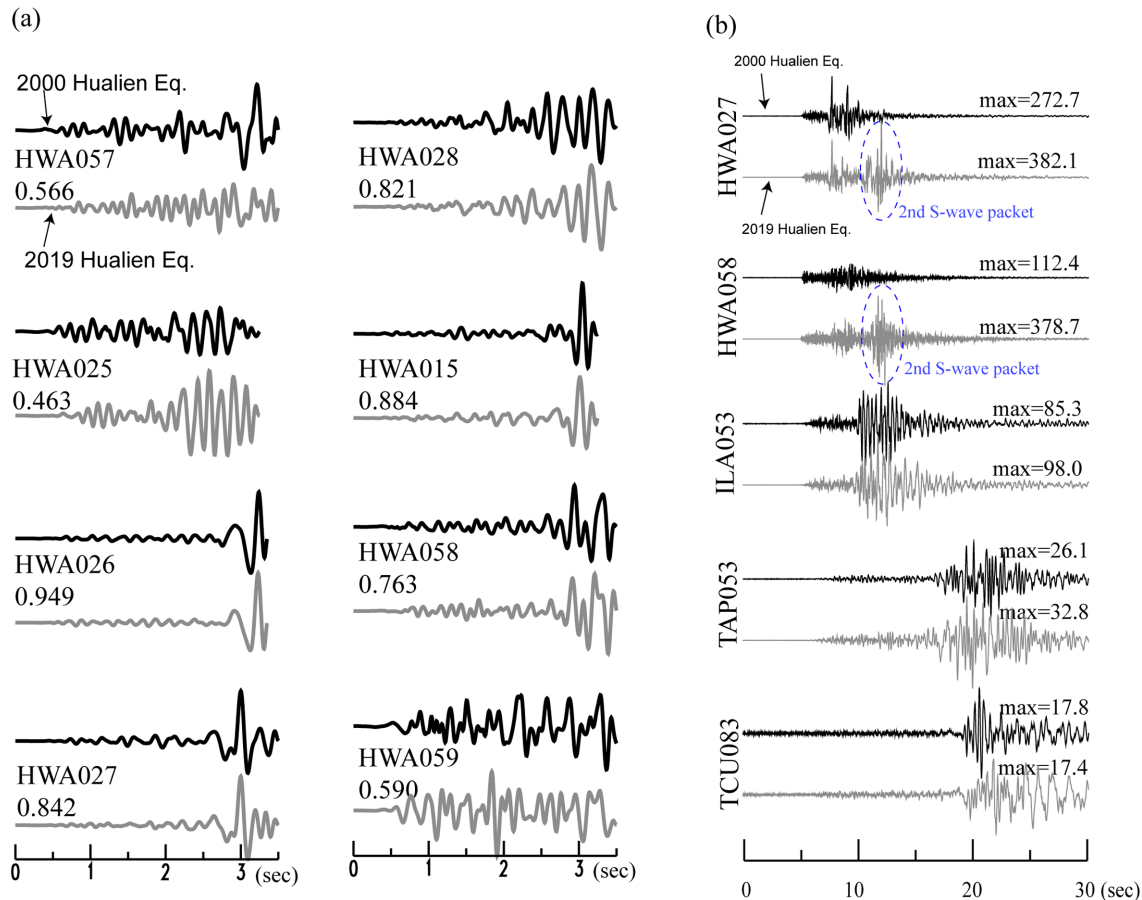
Figure 9. (a) Comparison of the 2–8 Hz bandpass filtered, EW-component waveforms for the 2000 (black lines) and 2019 (grey lines) Hualien events. The number under the station name represents the cross-correlation coefficient. (b) Comparison of the unfiltered EW-component waveforms for the 2000 (black lines) and 2019 (grey lines) Hualien events. The station locations are as shown in Fig. 1. The number above the traces indicates the maximum amplitudes of the observed records (cm s^{-2}).

Table 4. Parameters of the SMGA model for the 2000 Hualien earthquake determined by the strong ground motion simulation.

	M_0 (10^{17}Nm)	K	C	Rupture starting point	L (km)	W (km)	V_r (km s^{-1})	τ_r (s)	S (km^2)	SMGA (km^2)	$\Delta\sigma_{SMGA}$ (MPa)
SMGA	2.25	11	0.364	(8, 6)	1.65	2.2	3.13	0.55	38.24	3.63	24.4

2000 event, which is consistent with their SMGA models. We cannot analyse the SMGA for the 1986 event due to a lack of records. Here, we assume that its SMGA was close to its hypocentre, similar to the 2000 event.

Umino *et al.* (2006) analysed the locations of three *M*~7 Miyagi-oki earthquakes in the 1930s and the 1978 *M* = 7.4 Miyagi-oki earthquake and their aftershock. They concluded that the three events in the 1930s possibly ruptured a part of the source area of the 1978 event according to the partly overlapping aftershock areas. They also suggest that separate asperities could occasionally rupture in one large event or rupture separately at other times. In the present study, based on the close SMGAs and aftershock distributions of these M6 + events (Fig. 2b), we think that the M6 + earthquakes that occurred on the Xiulin segment in Taiwan are similar to the earthquakes that occurred in the Miyagi-oki area. The strong ground shaking of the moderate-sized events in the northern LV region may affect large areas of metropolises in northern Taiwan. It is necessary to raise concern and carry out more studies of this not-well-known but high-seismic-potential region. Rau *et al.* (2007) estimated that

the stored moment deficit for the northern LV region until 2006 corresponded to an *M*w 7.3 earthquake. However, the moment deficit accumulated continuously, and only a minor portion has been released by moderate-sized events since. This conclusion indicates that the probability of a future large earthquake remains high for the northern LV region.

5.3 Multiple SMGAs in Taiwan

Generally, events with multiple SMGAs are commonly found for large earthquakes due to the distinct wavepackets contributed from various asperities. For example, there are cases like the 2005 *M* 7.2 Miyagi-Oki earthquake (Suzuki & Iwata 2007), the 2008 *M*w 7.9 Wenchuan earthquake (Kurahashi & Irikura 2010), and the 2016 *M*w 7.0 Kumamoto earthquake (Irikura *et al.* 2017). On the other hand, moderate-sized earthquakes usually have only one SMGA, for example, the 1997 *M*6.5 Kagoshima-ken Hokuseibu earthquake (Miyake *et al.* 2003), the 2009 *M*w 6.3 L'Aquila earthquake (Poiata *et al.* 2012), and the 2010 *M*w 6.3 Jiashian and 2016 *M*w 6.4 Meinong
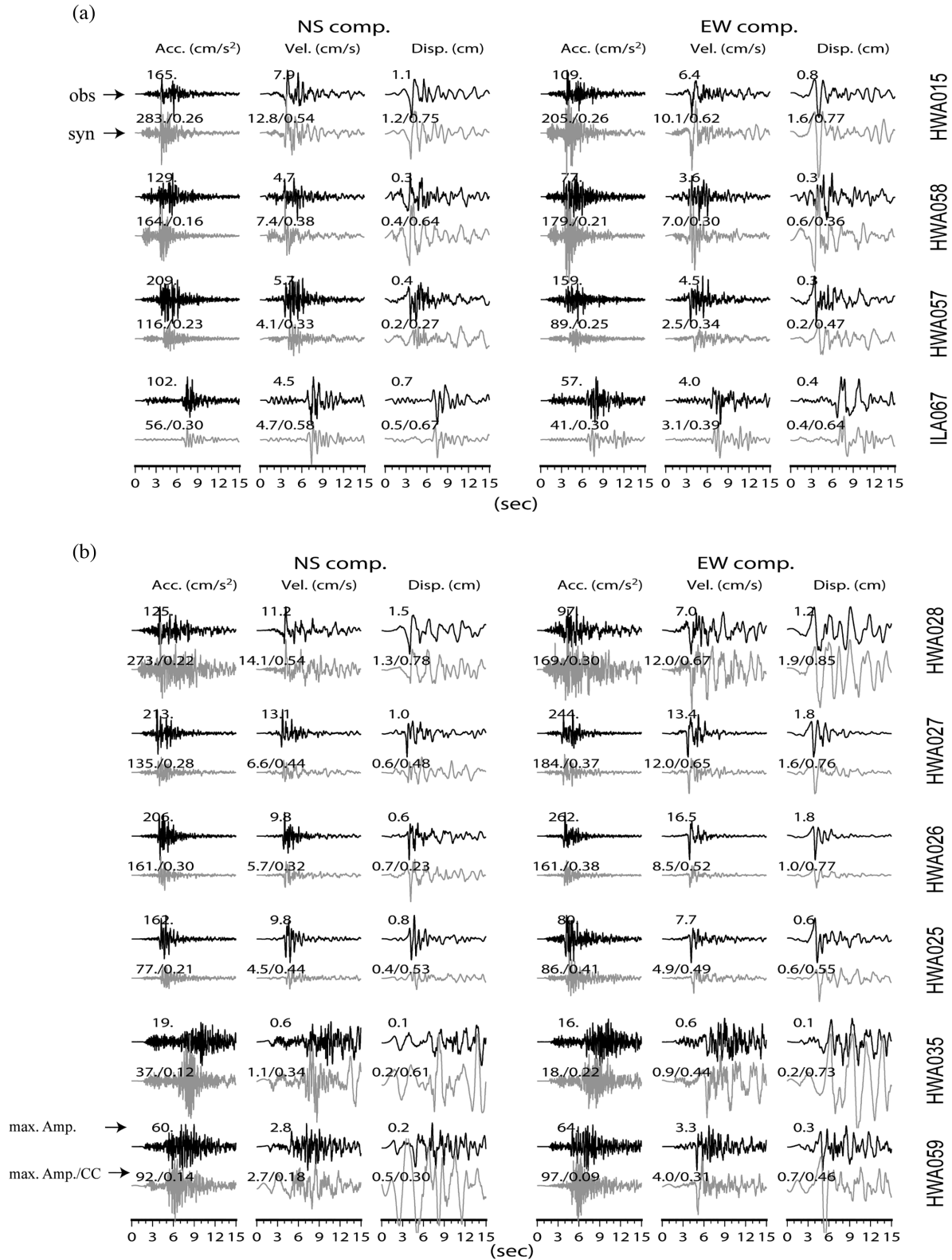
Figure 10. Comparison of observed (black lines) waveforms from the 2000 Hualien earthquake and synthetic (grey lines) waveforms at strong motion stations (a) used for source modelling in the empirical Green's function method and (b) used for forward ground motion simulations. The maximum amplitudes (max. Amp.) and the cross-correlation coefficient (CC) of the synthetic and the observed data are shown above the traces.

earthquakes (Wen *et al.* 2020). However, our results from the EGF method suggest that the 2019 event has two SMGA patches, with one near the CWB hypocentre and the other at the centroid location determined via the SSA approach. This source characteristic is

not similar to that of the other moderate earthquakes with only one SMGA in Taiwan (e.g. the 2013 Nantou earthquakes; the 2013 Ruisui and the 2014 Fanglin earthquakes; and the 2010 Jiashian and the 2016 Meinong earthquakes; Wen *et al.* 2014, 2016, 2020; Wen

2018). In this study, we report the first M6 event that has multiple SMGAs in Taiwan. The interaction between multiple SMGAs for a moderate earthquake needs further investigation in the future.

6 CONCLUSIONS

After analysing the records of the local strong motion networks, we found that the 2019 event initiates with small slips at the CWB hypocentre (SMGA1) and induces larger slips near the centroid location determined by the SSA approach (SMGA2). The centroid location is 5.5 km to the north-northwest of and 3.8 km deeper than the CWB hypocentre, suggesting that the high-angle west-dipping plane of the focal solution was the rupture plane of the 2019 event. The areas of both SMGAs are relatively small compared to the empirical relationship of Somerville *et al*. (1999), which reveals that the high stress drops of SMGA1 and SMGA2 are 13.7 and 27.4 MPa, respectively. Such a high stress drop on the asperities, along with the strong directivity effect coupled with the radiation pattern from the finite-fault model (Lee *et al*. 2020), are some of the essential factors for generating the large PGA locally and in northern Taiwan.

Based on the similarities of waveform characteristics, source parameters, and strong ground motion patterns, we inferred that three M6 + earthquakes of the 1986, 2000 and 2019 events in the Xiulin segment have similar source properties, with a high stress drop on SMGAs generating the large PGA locally and widely affecting the metropolises in northern Taiwan. Considering the stored moment deficit, the probability for a future large earthquake in the northern LV region remains high. In accordance with the potential threat of strong motion, it is important to raise concern about seismic hazard assessment and mitigation for this not-well-known but high-seismic-potential region. The Xiulin segment is one of the hot zones.

DATA AVAILABILITY

The strong-motion records used in this study were obtained from the National Taiwan University (NTU) and the Central Weather Bureau (CWB). The P-Alert records used in this study are available to the public and can be downloaded from the NTU cloud disc (http://palert.earth.sinica.edu.tw/db/). The strong-motion records from CWB used in this study can be obtained upon request from the Geophysical Database Management System (GDMS; https://gdms.cwb.gov.tw/).

CONFLICT OF INTEREST

The authors declare that they have no known competing financial interests or personal relationships that could have appeared to influence the work reported in this paper.

REFERENCES

Asano, K. & Iwata, T., 2011. Characterization of stress drops on asperities estimated from heterogeneous kinematic slip model for strong motion prediction for inland crustal earthquakes in *Japan*, *Pure appl. Geophys.,* **168,** 105–116.

Asano, K., Iwata, T. & Irikura, K., 2003. Source characteristics of shallow intraslab earthquakes derived from strong-motion simulations, *Earth Planets Space,* **55,** e5–e8.

Brune, J.N., 1970. Tectonic stress and the spectra of seismic shear waves from earthquakes, *J. geophys. Res.,* **75,** 4997–5009.

Brune, J.N., 1971. Correction, *J. geophys. Res.,* **76,** 5002.

CEOC, 2019. The broad of the earthquake disaster (10804181600) (in Chinese), Retrieved from https://www.emic.gov.tw/9/index.php?code=list&ids=381&detail=98

Chan, C.H., Wang, Y., Wang, Y.J. & Lee, Y.T., 2017. Seismic-hazard assessment over time: modeling earthquakes in Taiwan, *Bull. seism. Soc. Am.,* **107**(5), 2342–2352.

Chan, C.H., Ma, K.F., Lee, Y.T. & Wang, Y.J., 2019. Rethinking seismic source model of probabilistic hazard assessment in Taiwan after the 2018 Hualien, Taiwan, earthquake sequence, *Seismol. Res. Lett.,* **90**(1), 88–96.

Chen, K.H., Toda, S. & Rau, R.J., 2008. A leaping, triggered sequence along a segmented fault: the 1951 Hualien–Taitung earthquake sequence in eastern Taiwan, *J. geophys. Res.,* **113,** B02304, doi:10.1029/2007JB005048.

Chen, Y., Chen, K.H., Hu, J.C. & Lee, J.C., 2020. Probing variation in aseismic slip behavior in a reverse fault system: observation from repeating earthquakes in eastern Taiwan, *J. geophys. Res.,* **124,** doi:10.1029/2019JB018561.

Ching, K.E., Rau, R.J. & Zeng, Y., 2007. Coseismic source model of the 2003 M_w 6.8 Chengkung earthquake, Taiwan, determined from GPS measurements, *J. geophys. Res.,* **112,** B06422, doi:10.1029/2006JB004439.

Cotton, F., Archuleta, R. & Causse, M., 2013. What is the sigma of the stress drop? *Seismol. Res. Letts.,* **84,** 42–48.

Hickman, J.B., Wiltschko, D.V., Hung, J.H., Fang, P. & Bock, Y., 2002. Structure and evolution of the active fold-and-thrust belt of southwestern Taiwan from global positioning system analysis, in *Geology and Geophysics of an Arc-Continent Collision, Taiwan,* Vol. 358, pp. 75–92, eds Byrne, T.B. & Liu, C.S., Spec. Pap. Geol. Soc. Am.

Huang, H. H, Wu, Y.M., Song, X., Chang, C.H., Lee, S.J., Chang, T.M. & Hsieh, H.H., 2014. Joint Vp and Vs tomography of Taiwan: implications for subduction-collision orogeny, *Earth planet. Sci. Lett.,* **392,** 177–191.

Huang, M.H. & Huang, H.H., 2018. The complexity of the 2018 M_w 6.4 Hualien earthquake in east Taiwan, *Geophys. Res. Lett.,* **45**(24), 13–249.

Irikura, K., 1986. Prediction of strong acceleration motions using empirical Green's function, in *Proceedings of 7th Japan Earthquake Engineering Symp.,* pp. 151–156, Tokyo.

Irikura, K. & Kamae, K., 1994. Estimation of strong ground motion in broad-frequency band based on a seismic source scaling model and an empirical Green's function technique, *Ann. Geophys.,* **37,** 1721–1743.

Irikura, K. & Miyake, H., 2011. Recipe for predicting strong ground motion from crustal earthquake scenarios, *Pure appl. Geophys.,* **168,** 85–104.

Irikura, K., Miyakoshi, K., Kamae, K., Yoshida, K., Somei, K., Kurahashi, S. & Miyake, H., 2017. Applicability of source scaling relations for crustal earthquakes to estimation of the ground motions of the 2016 Kumamoto earthquake, *Earth Planets Space,* **69,** 10.

Kan, C.W., Kao, H., Ou, G.B., Chen, R.Y. & Chang, C.H., 2010. Delineating the rupture planes of an earthquake doublet using Source-Scanning Algorithm: application to the 3 March 2005 Ilan doublet, northeast Taiwan, *Geophys. J. Int.,* **182,** 956–966.

Kao, H. & Shan, S.J., 2004. The Source-Scanning Algorithm: mapping the distribution of seismic sources in time and space, *Geophys. J. Int.,* **157,** 589–594.

Kao, H. & Shan, S.J., 2007. Rapid identification of earthquake rupture plane using Source-Scanning Algorithm, *Geophys. J. Int.,* **168,** 1011–1020.

Kao, H., Wang, K., Chen, R.Y., Wada, I., He, J. & Malone, S.D., 2008. Identifying the rupture plane of the 2001 Nisqually, Washington, earthquake, *Bull. seism. Soc. Am.,* **98,** 1546–1558.

Kuo, C.H., Huang, J.Y., Lin, C.M., Hsu, T.Y., Chao, S.H. & Wen, K.L., 2019. Strong ground motion and pulse-like velocity observations in the near-fault region of the 2018 M_w 6.4 Hualien, Taiwan, earthquake, *Seismol. Res. Lett.,* **90**(1), 40–50.

Kurahashi, S. & Irikura, K., 2010. Characterized source model for simulating strong ground motions during the 2008 Wenchuan earthquake, *Bull. seism. Soc. Am.,* **100**(5B), 2450–2475.

Lee, S.J., Huang, H.H., Shyu, J.B.H., Yeh, T.Y. & Lin, T.C., 2014. Numerical earthquake model of the 31 October 2013 Ruisui, Taiwan, earthquake: source rupture process and seismic wave propagation, *J. Asian Earth Sci.,* **96,** 374–385.

Lee, S.J., Lin, T.C., Liu, T.Y. & Wong, T.P., 2019. Fault-to-fault jumping rupture of the 2018 M_w 6.4 Hualien earthquake in eastern Taiwan, *Seismol. Res. Lett.,* **90**(1), 30–39.

Lee, S.J., Wong, T.P., Liu, T.Y., Lin, T.C. & Chen, C.T., 2020. Strong motion over a large area in northern Taiwan caused by the northward rupture directivity of the 2019 Hualien earthquake, *J. Asian Earth Sci.,* **192,** 104095.

Liao, Y.-C., Kao, H., Rosenberger, A., Hsu, S.K. & Huang, B.S., 2012. Delineating complex spatiotemporal distribution of earthquake aftershocks: an improved Source-Scanning Algorithm, *Geophys. J. Int.,* **189,** 1753–1770.

Lin, Y.Y., Yeh, T.Y., Ma, K.F., Song, T.R.A., Lee, S.J., Huang, B.S. & Wu, Y.M., 2018. Source characteristics of the 2016 Meinong (M_L 6.6), Taiwan, earthquake, revealed from dense seismic arrays: double sources and pulse-like velocity ground motion, *Bull. seism. Soc. Am.,* **108,** 188–199.

Lin, Y.Y., Kanamori, H., Zhan, Z., Ma, K.F. & Yeh, T.Y., 2020. Modelling of pulse-like velocity ground motion during the 2018 M_w 6.3 Hualien earthquake, Taiwan, *Geophys. J. Int.,* **223**(1), 348–365.

Liu, K.S. & Tsai, Y.B., 2005. Attenuation relationships of peak ground acceleration and velocity for crustal earthquakes in Taiwan, *Bull. seism. Soc. Am.,* **95**(3), 1045–1058.

Liu, K.S., Shin, T.C. & Tsai, Y.B., 1999. A free-field strong motion network in Taiwan: TSMIP, *Terr. Atmos. Ocean. Sci.,* **10**(2), 377–396.

Lo, Y.C., Yue, H., Sun, J., Zhao, L. & Li, M., 2019. , *Earth planet. Sci. Lett.,* **524,** 115729.

Miyake, H., Iwata, T. & Irikura, K., 1999. Strong ground motion simulation and source modeling of the Kagoshima-ken Hokuseibu earthquakes of March 26 (M_{JMA} 6.5) and May 13 (M_{JMA} 6.3), 1997, using empirical Green's function method, *Zisin,* **51,** 431–442 (in Japanese with English abstract).

Miyake, H., Iwata, T. & Irikura, K., 2001. Estimation of rupture propagation direction and strong motion generation area from azimuth and distance dependence of source amplitude spectra, *Geophys. Res. Lett.,* **28,** 2727–2730.

Miyake, H., Iwata, T. & Irikura, K., 2003. Source characterization for broadband ground-motion simulation: kinematic heterogeneous source model and strong motion generation area, *Bull. seism. Soc. Am.,* **93,** 2531–2545.

NCREE, 2019. The earthquake disaster report of the Hualien Sioulin earthquake (in Chinese), retrieved from https://www.ncree.org/EarthquakeInfo/20190418/2019%E5%B9%B44%E6%9C%8818%E6%97%A5%E8%8A%B1%E8%93%AE%E7%A7%80%E6%9E%97%E5%9C%B0%E9%9C%87%E7%81%BD%E6%83%85%E5%BD%99%E6%95%B4%E5%A0%B1%E5%91%8A_0503.pdf.

Poiata, N., Koketsu, K., Vuan, A. & Miyake, H., 2012. Low-frequency and broad-band source models for the 2009 L'Aquila, Italy, earthquake, *Geophys. J. Int.,* **191,** 224–242.

Radiguet, M., Cotton, F., Manighetti, I., Campillo, M. & Douglas, J. 2009. Dependency of near-field ground motions on the structural maturity of the ruptured faults, *Bull. seism. Soc. Am.,* **99,** 2572–2581.

Rau, R.J., Chen, K.H. & Ching, K.E., 2007. Repeating earthquakes and seismic potential along the northern Longitudinal Valley fault of eastern Taiwan, *Geophys. Res. Lett.,* **34,** L24301, doi:10.1029/2007GL031622.

Somerville, P. *et al.*, 1999. Characterizing crustal earthquake slip models for the prediction of strong ground motion, *Seismol. Res. Lett.,* **70,** 59–80.

Somerville, P.G., 2003. Magnitude scaling of the near fault rupture directivity pulse, *Phys. Earth planet Inter.,* **137,** 201–212.

Su, L., 2019. The Malaysian who was seriously injured in the 418 Hualien earthquake passed away, *The Central News Agency*, 28 Apr. 2019, https://www.cna.com.tw/news/firstnews/201904280133.aspx.

Suzuki, W. & Iwata, T., 2007. Source model of the 2005 Miyagi-Oki, Japan, earthquake estimated from broadband strong motions, *Earth Planets Space,* **59,** 1155–1171.

Tsai, C.C., Yeh, Y.T., Wen, K.L., Cheng, S.N. & Kao, M.H., 1986. The Hualien earthquake of May 20, 1986: strong ground motion data and response spectra, *Bull. Inst. Earth Sci. Acad. Sin.,* **6,** 29–64.

Umino, N. *et al.*, 2006. Revisiting the three $M\sim7$ Miyagi-oki earthquakes in the 1930s: possible seismogenic slip on asperities that were re-ruptured during the 1978 $M = 7.4$ Miyagi-oki earthquake, *Earth Planets Space,* **58,** 1587–1592.

Wang, Y.J., Chan, C.H., Lee, Y.T., Ma, K.F., Shyu, J.B.H., Rau, R.J. & Cheng, C.T., 2016. Probabilistic seismic hazard assessment for Taiwan, *Terr. Atmos. Ocean. Sci.,* **27**(3), 325–340.

Wen, Y.Y., 2018. Source characteristics of the northern Longitudinal Valley, Taiwan derived from broadband strong-motion simulation, *Pure appl. Geophys.,* **175,** 587–596.

Wen, Y.Y., Miyake, H., Yen, Y.T., Irikura, K. & Ching, K.E., 2014. Rupture directivity effect and stress heterogeneity of the 2013 Nantou blind-thrust earthquakes, Taiwan, *Bull. seism. Soc. Am.,* **104,** 2933–2942.

Wen, Y.Y., Yen, Y.T., Wen, S., Lee, S.J., Kuo, C.H. & Lin, Y.Y., 2016. Hybrid ground motion simulation for the 2013 M_L 6.4 Ruisui, Taiwan earthquake, *Terr. Atmos. Ocean. Sci.,* **27,** 407–414.

Wen, Y.Y., Chao, S.Y., Yen, Y.T. & Wen, S., 2017. Source characteristics of moderate-to-strong earthquakes in the Nantou area, Taiwan: insight from strong ground motion simulations, *Earth Planets Space,* **69,** doi:10.1186/s40623-017-0720-5.

Wen, Y.Y., Wen, S., Lee, Y.H. & Ching, K.E., 2019. The kinematic source analysis for 2018 M_w 6.4 Hualien, Taiwan earthquake, *Terr. Atmos. Ocean. Sci.,* **30,** 377–387.

Wen, Y.Y., Yen, Y.T., Kuo, C.H. & Ching, K.E., 2020. Source and strong–motion characteristics of two $M >6$ buried earthquakes in southwest Taiwan, *Earth Planets Space,* **72,** doi:10.1186/s40623-020-01322-y.

Wu, Y.M., Chen, D.Y., Lin, T.L., Hsieh, C.Y., Chin, T.L., Chang, W.Y., Li, W.S. & Ker, S.H., 2013. A high-density seismic network for earthquake early warning in Taiwan based on low cost sensors, *Seismol. Res. Lett.,* **84,** 1048–1054.

Yen, Y.T. & Ma, K.F., 2011. Source-scaling relationship for $M4.6$–8.9 earthquakes, specifically for earthquakes in the collision zone of Taiwan, *Bull. seism. Soc. Am.,* **101,** 468.

Yu, S.B. & Kuo, L.C., 2001. Present-day crustal motion along the Longitudinal Valley Fault, eastern Taiwan, *Tectonophysics,* **333,** 199–217.

APPENDIX A:

To measure the uncertainty of the centroid location estimated by the SSA approach, we consider nine grids with the largest spatial probabilities as potential locations. The cumulative probability of these grids is 91.26 per cent (Fig. A1a), suggesting that the
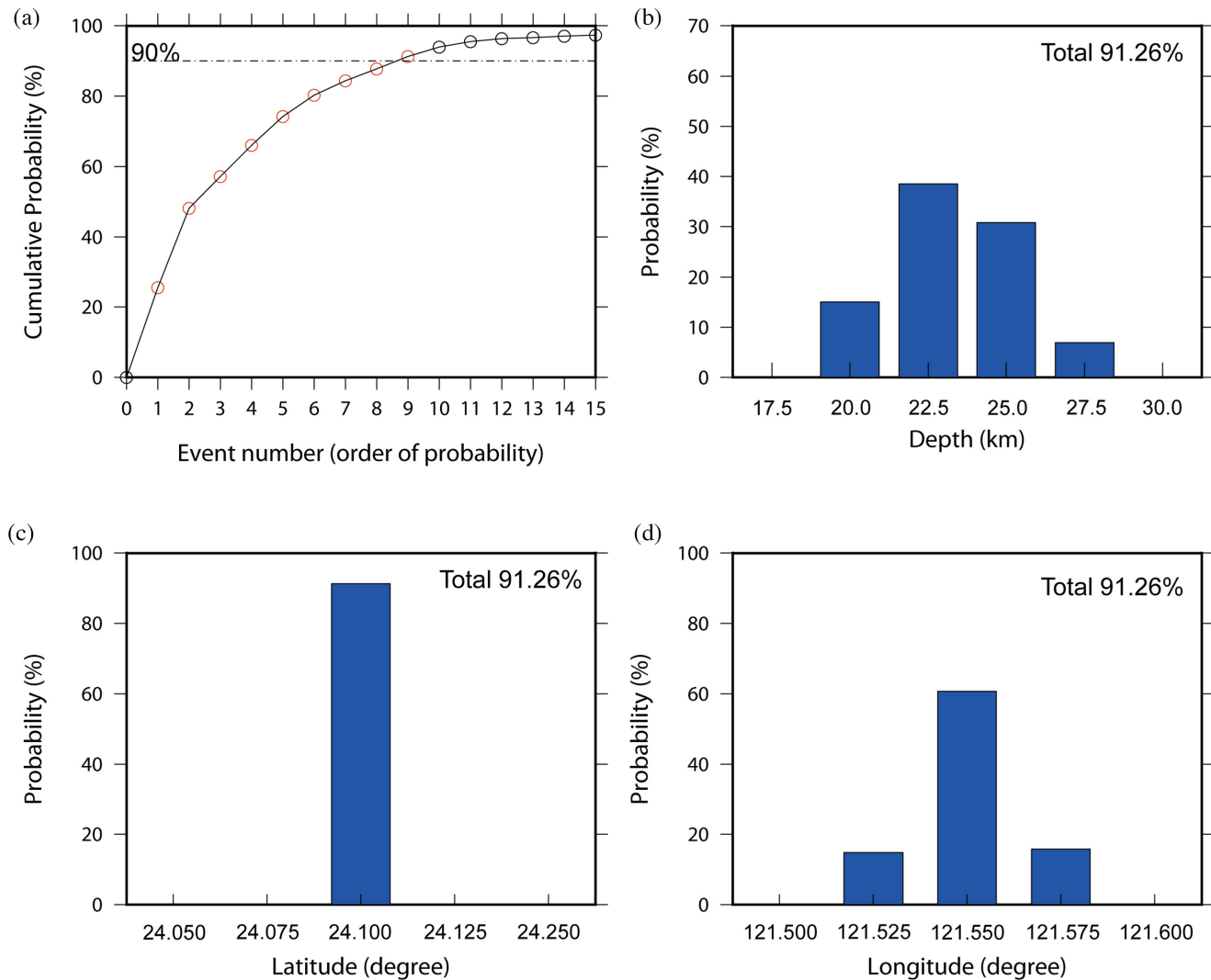
Figure A1. Uncertainty of the centroid location. (a) Spatial cumulative probability plotted against event number ordering of spatial individual probability. The dashed line shows the 90 per cent cumulative probability. The red circles indicate the events we considered for the uncertainty estimation. The cumulative probability is 91.26 per cent. Probability distributions are shown along with depth, latitude and longitude in (b)–(d), respectively.

earthquake has a 91.26 per cent chance of being located inside the grids. Figs A1(b)–(d) indicate the probability summation for these grids in depth, latitude and longitude. The results show more confidence in the horizontal location than in depth. The uncertainty in depth is from 20 to 27.5 km, and the uncertainties in latitude and longitude are ± 1.25 km (one grid) and ± 2.5 km (two grids), respectively.

APPENDIX B:

Based on the ω^{-2} source spectral model of Brune (1970, 1971), the observed source spectral ratio of the target event to the EGF event is fitted by a theoretical function curve (Miyake *et al.* 1999, 2003):

$$\text{SSRF}(f) = \frac{M_0}{m_0} \cdot \frac{1 + \left(\frac{f}{f_{ca}}\right)^2}{1 + \left(\frac{f}{f_{cm}}\right)^2}. \tag{B1}$$

M_0 and m_0 are the seismic moments of the target and EGF events, respectively. f_{cm} and f_{ca} are the corner frequencies of the target and EGF events, respectively. The scaling parameters C and K, which are the ratios of the stress drops and fault dimensions between the target event and the EGF event, can be derived by applying the formulae of Irikura (1986) and Miyake *et al.* (2003):

$$U_0/u_0 = M_0/m_0 = CK^3, \quad K = f_{ca}/f_{cm}, \tag{B2}$$

U_0/u_0 is the flat level of the displacement spectra ratio of the target-to-EGF events in the low-frequency range. Considering the probable rupture directivity effect, four strong-motion stations surrounding the source region (open squares in Fig. 3) are chosen for the source spectral ratio analysis in the broad-band frequency range (0.4–10 Hz).

Using the procedure of the single-SMGA model as an example, Fig. B1 shows the observed and fitted spectral ratios of the 2019 Hualien event to the EGF event. Through the source spectral
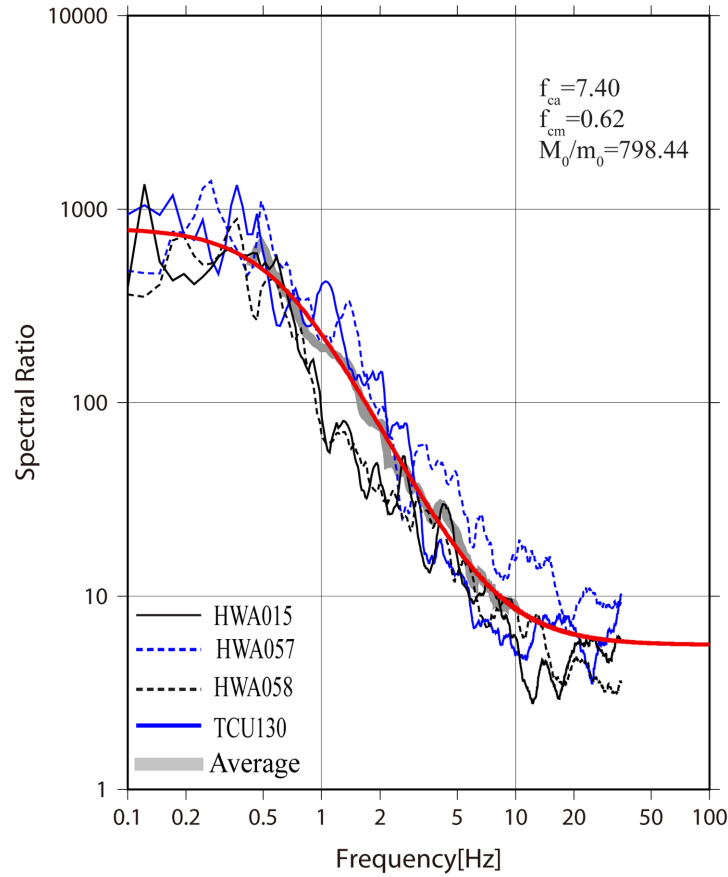
Figure B1. Observed source spectral ratios of the stations used for the source modelling, the average observed source spectral ratio (thick grey line) and fitting source spectral ratio function (red line) for the 2019 Hualien event. The values of the parameters determined from the source spectral ratio fitting are listed.

ratio fitting analysis, we obtain the scaling parameters $K = 12$ and $C = 0.470$. We then apply the EGF method to estimate the SMGA, which is defined as $K \times K$ subfaults with dimensions equivalent to the rupture area of the EGF event (Irikura 1986; Irikura & Kamae 1994; Miyake *et al.* 2001). Through the grid search, the optimal SMGA-related parameters, including the initiation position (rupture starting point), width (W) and length (L) of the SMGA, rupture velocity (V_r) and rise time (τ_r), are then determined by minimizing the fitting residuals of displacement records and the acceleration envelopes (Miyake *et al.* 1999):

$$\text{residual} = \frac{\sum_t \left(u_{\text{obs}} - u_{\text{syn}}\right)^2}{\sqrt{\left(\sum_t u_{\text{obs}}^2\right)\left(\sum_t u_{\text{syn}}^2\right)}}$$
$$+ \frac{\sum_t \left(a_{\text{env, obs}} - a_{\text{env,syn}}\right)^2}{\left(\sum_t a_{\text{env,obs}}\right)\left(\sum_t a_{\text{env,syn}}\right)}. \tag{B3}$$

u_{obs} and u_{syn} represent the observed and synthetic displacements. $a_{\text{env, obs}}$ and $a_{\text{env,syn}}$ are the observed and synthetic acceleration envelopes.